Journal of Solid State Chemistry 332 (2024) 124590

Contents lists available at ScienceDirect

Journal of Solid State Chemistry

journal homepage: www.elsevier.com/locate/jssc

Effect of W and Mo co-substitution on conductivity and structure of $LaNbO_4$

Yidong Han [a,1], Siqi Li [a,b,1], Stephen Skinner [a,*]

[a] Department of Materials, Imperial College London, SW7 2AZ, London, United Kingdom
[b] Department of Chemistry, Technical University of Munich, Garching, 85748, Munich, Germany

ARTICLE INFO

Keywords:
$LaNbO_4$
W and Mo co-doping
Modulated structure
Oxide ion conductivity

ABSTRACT

$LaNb_{1-x}M_xO_{4+\delta}$ (M = W, Mo) which adopts a modulated tetragonal scheelite type structure exhibits enormous potential as an electrolyte material for solid oxide fuel cells. Here we report the solid-state synthesis of a series of W/Mo co-substituted samples with $LaNb_{0.8}W_xMo_{0.2-x}O_{4.1}$ (x = 0.00, 0.02, 0.04, 0.10, 0.16, 0.18, 0.20) which exhibited the highest total conductivity at x = 0.02 in the intermediate temperature range (2.37×10^{-3} S cm^{-1} at 665 °C in air). Powder X-ray diffraction patterns showed that the tetragonal phases were able to be stabilized at room temperature when x > 0.02. The phase diagram obtained from variable-temperature X-ray diffraction, indicated that the modulated structures could be maintained from room temperature to 900 °C when x ≥ 0.10. With the combination of electrochemical impedance spectroscopy measurements and Rietveld refinements from X-ray diffraction patterns, total conductivities of these materials were found to be proportional to the volume of the unit cells. It is also noted that the existence of modulated structures negatively impacts the total conductivities.

1. Introduction

Solid oxide fuel cells (SOFCs) are regarded as electrochemical devices with high efficiency that successfully convert chemical energy in gaseous fuels to electrical energy with only environmentally-friendly by-products, theoretically water when a green hydrogen source is utilized [1]. Applications of SOFCs have been identified from small portable electrical devices to large-scale facilities including data centres, domestic and district combined heat and power [2]. As cell technology matures, there have been increasing demands for increased lifetime leading to further optimisation of the electrochemical performance of SOFCs [3]. A critical component of the SOFC is the electrolyte material that acts as the ionic conducting membrane, providing gas separation and contributing to the Ohmic resistance of the cell [4]. Typically, cells have been operated at increased temperature to reduce the contribution of Ohmic resistance from the electrolyte [5]. Operating at high temperatures inevitably leads to increased degradation and reduced lifetime [6]. In order to overcome this limitation there has been a drive to reduce operating temperatures, which leads to either reducing the electrolyte thickness or developing new high performance electrolyte materials [1,7]. In this circumstance, a material possessing high ionic conductivity at low temperature is ideal for a competitive electrolyte in SOFCs [8].

The $CeNbO_{4+\delta}$ phase, adopting modulated crystal structures, is one type of alternative material which exhibits a remarkable oxide ion diffusion coefficient (D* = 1.26×10^{-7} cm^2 s^{-1} at 650 °C) in the low working temperature range of SOFCs, presenting great competitiveness in utilization of solid electrolytes [9]; however, the oxidation of Ce^{3+} ions reduces the oxygen diffusion coefficient and chemical stability, as well as introducing electronic charge carriers, thus hindering its application [10]. With a similar structure as $CeNbO_{4+\delta}$, donor doped $LaNbO_4$ has been studied as a potential electrolyte material [11].

$LaNbO_4$ possesses a monoclinic fergusonite (I2/a) structure at room temperature and experiences a phase transition to the tetragonal scheelite ($I4_1/a$) structure at elevated temperature (around 450 °C) [12]. The tetragonal scheelite structure is formed by LaO_8 and NbO_4 units locating at edges and corners, respectively with isotropic oxygen sites [13]. The remarkable oxide ion transportation of the tetragonal phase is ascribed to the contribution of both interstitial and lattice oxygen species [14]. Density functional theory (DFT) calculations revealed that tetragonal $LaNbO_4$ possesses three isotropic ion diffusion pathways [14] while only one diffusion pathway along the b axis exists in monoclinic $LaNbO_4$ [15]. Donor doping on the Nb site is proposed to benefit ionic conductivity for oxide ion transportation [16], reducing phase transition temperature, and introducing modulated structures

* Corresponding author.
E-mail address: s.skinner@imperial.ac.uk (S. Skinner).
[1] Yidong Han and Siqi Li both contributed equally to this work.

https://doi.org/10.1016/j.jssc.2024.124590
Received 5 December 2023; Received in revised form 30 January 2024; Accepted 31 January 2024
Available online 1 February 2024

[17].

$LaNb_{1-x}W_xO_{4+\delta}$, where Nb^{5+} ions are partially substituted by W^{6+}, becomes competitive due to the combination of chemical stability and thermal expansion coefficient matching typical electrode materials [16]. Also, substitution levels from 8 % to 16 % of W could enhance the total conductivity (3.0×10^{-3} S cm^{-1} at 800 °C in compressed air) by 1.5 orders of magnitude compared with $LaNbO_4$ [18]. The phase transition temperature significantly decreased as well, while 16 % W-substituted samples possess a tetragonal scheelite structure at room temperature [17]. Modulated structures can be observed in selected area election diffraction (SAED) patterns which were indexed by 5 independent vectors, which is recognized as a (3 + 2) D incommensurate structure [19]. Combined with X-ray diffraction (XRD) results, DFT calculations indicated that the Nb tetrahedra were distorted by modulated structures introduced with W substitution, and the coordination number of Nb near oxygen interstitials increased from 4 to 6–8 [19], which is verified by ^{93}Nb nuclear magnetic resonance (NMR) spectra [17]. However, the simulation results from Toyoura *et al* indicated that W^{6+} substitution tends to trap oxide ions on La sites, hindering ion transportation [14]. In this case, another strategy has been proposed, which is utilizing Mo^{6+} as the substituent ion on Nb sites, where the DFT results verify the Mo^{6+} occupied on Nb sites possesses reduced association energy [14] with suppressed trapping effect. 20 % Mo substituted $LaNbO_4$ has been proven to have three orders of magnitude higher total conductivity (2.65×10^{-2} S cm^{-1} at 900 °C in compressed air) than $LaNbO_4$ [20]. Additionally, modulated structures were also observed in Mo substituted samples and the SAED patterns of 10 % Mo substituted $LaNbO_4$ indicated the modulated structure is a (3 + 2) D incommensurate structure [15,21]. However, the phase transition temperatures of Mo substituted samples are higher than the W substituted samples [15,17]. To possess both high conductivity and low phase transition temperature, a strategy of co-substituting Mo and W is suggested. Similar approaches have been successful in previous research, such as doping Ce and Yb on La sites [22] or co-substituting W and Mo on metallic oxides [23].

In this contribution, we focus on structural changes and correlating electrochemical performance of a series of co-substituted samples $LaNb_{0.8}W_xMo_{0.2-x}O_{4.1}$ (x = 0.00, 0.02, 0.04, 0.10, 0.16, 0.18, 0.20) and propose possible mechanisms. The phase diagram of co-substituted samples in the temperature ranges from 25 °C to 900 °C was generated by variable-temperature XRD, especially concentrating on the emergence and absence of modulated structures. The modulated structure was also indexed from the SAED patterns. The relationship between lattice parameters and total conductivities were investigated, and the impact of modulated structures was discussed.

2. Experimental details

2.1. Sample preparation

The synthesis of ceramic samples was conducted by the solid state reaction route using La_2O_3 (99.9 %, Sigma-Aldrich), Nb_2O_5 (99.9 %, Sigma-Aldrich), MoO_3 (99.5 %, Sigma-Aldrich), and WO_3 (99.8 %, Alfa Aesar) as starting materials. Co-substituted samples of composition $LaNb_{0.8}W_xMo_{0.2-x}O_{4.1}$ (x = 0.00, 0.02, 0.04, 0.10, 0.16, 0.18, 0.20) were prepared and subsequently denoted as $LNMo_{20}$, LNW_2Mo_{18}, LNW_4Mo_{16}, $LNW_{10}Mo_{10}$, $LNW_{16}Mo_4$, $LNW_{18}Mo_2$, and LNW_{20}, respectively. Note all oxygen stoichiometries discussed are the nominal values (4.1) assuming all cations adopt their common valence states: La^{3+}, Nb^{5+}, W^{6+} and Mo^{6+}. The powder mixtures were ground in a mortar and pestle for at least 30 min by hand with acetone to maximise homogeneity. The ground powders were then transferred to an alumina crucible and calcined under static air at 1000 °C for 10 h, with a heating rate of 5 °C/min, then cooled to room temperature with the same rate. Due to the requirement of subsequent electrochemical tests, the as calcined powders were pressed into pellets with 13 mm diameter before sintering. 1g powder was weighed for each pellet and uniaxially pressed at 5 tons for 5 min. Then, the pellets were transferred to an alumina crucible for sintering at 1400 °C for 10 h with a heating rate of 5 °C/min and cooled to room temperature with the same rate. To avoid any possible volatilisation of Mo or W during the sintering process, the pellets were buried in the calcined powder with same chemical composition.

2.2. Sample characterization

To determine the phase evolution and lattice parameters, variable-temperature X-ray diffraction (VT-XRD) was utilized. Both room temperature (25 °C) and variable-temperature diffraction patterns were collected by XRD (Empyrean, PANalytical) with Cu Kα radiation (λ = 1.5406 Å with an Anton Parr HTK1200 chamber. The 2θ range was from 10° to 90° with a step size of 0.034°. The temperature range for VT-XRD was from 50 °C to 900 °C, measuring at 50 °C intervals. The XRD patterns were then evaluated using Rietveld refinement using the GSAS II software package [24], extracting the lattice parameters. The morphology of the as-sintered samples was investigated by scanning electron microscopy (SEM, Leo Gemini-1525, Zeiss). The chemical compositions of all samples were analysed by Energy Dispersive X-Ray spectroscopy (EDX, X-Max/Auriga, Oxford instrument/Zeiss). The selected area electron diffraction (SAED) patterns of the as-sintered LNW_2Mo_{18} and $LNW_{18}Mo_2$ powders were obtained by transmission electron microscopy (TEM, JEM-2100Plus, JEOL).

Before electrochemical impedance spectroscopy (EIS) measurement, the shaped and sintered pellets were coated with gold paste on both sides. Then, the coated pellets were heated for 1 h at 900 °C so that the gold layer can be tightly connected with the pellets. The EIS tests were conducted using a Solartron 1260 frequency response analyzer (FRA) in compressed air, over the temperature range from 600 °C to 900 °C, controlled by SMaRT impedance measurement software (SMaRT, v 3.3.0, Solartron analytical). The AC potential was 100 mV and frequencies were tested from 1 MHz to 500 mHz. The obtained impedance spectra were fitted using the ZView package (v4.0b, Scribner Associates).

3. Results and discussion

3.1. Structural evolution of $LaNb_{0.8}W_xMo_{0.2-x}O_{4.1}$ series

Fig. 1 displays the X-ray diffraction patterns of $LaNb_{0.8}W_xMo_{0.2-x}O_{4.1}$ at room temperature. Synthesised samples were single phase at room temperature, and only low-level of impurities were observed in samples with high W concentration, identified as $La_2W_2O_9$. Aside from $LNMo_{20}$ and LNW_2Mo_{18} which maintained a monoclinic fergusonite phase, other samples with increasing W concentration were transformed into tetragonal scheelite phases at room temperature. The two split main peaks merged into one (around 28.1° 2θ) with the transition from a monoclinic to tetragonal phase, shown in the top right corner in Fig. 1. Noticeably, the modulated structures existed in all samples at room temperature (referring to the peak at around 26.7° 2θ). The diffraction patterns indicated that co-doping of W and Mo facilitated the reduction of the phase transition temperature and emergence of modulated structures.

The structures of $LaNb_{0.8}W_xMo_{0.2-x}O_{4.1}$ were investigated by conducting Rietveld refinements of the diffraction data measured at room temperature, represented in Fig. 2 (a) with the results of $LNW_{16}Mo_4$ as an example; Table S1 summarizes the refined parameters for all materials. Modulated structures were not considered in the refinements. Lattice parameters of different compositions are summarized in Fig. 2 (b) and **(c)**, where the spots related to $LNMo_{20}$ and LNW_2Mo_{18} are marked as monoclinic phase. Apart from the monoclinic $LNMo_{20}$ and LNW_2Mo_{18} compositions, the *c* lattice parameter increased with W fraction increasing from 0.04 to 0.16, reaching a plateau beyond this composition. The increase of *c* lattice parameter was expected as Mo^{6+} ions with smaller radius (0.41 Å in 4-coordinate) were gradually

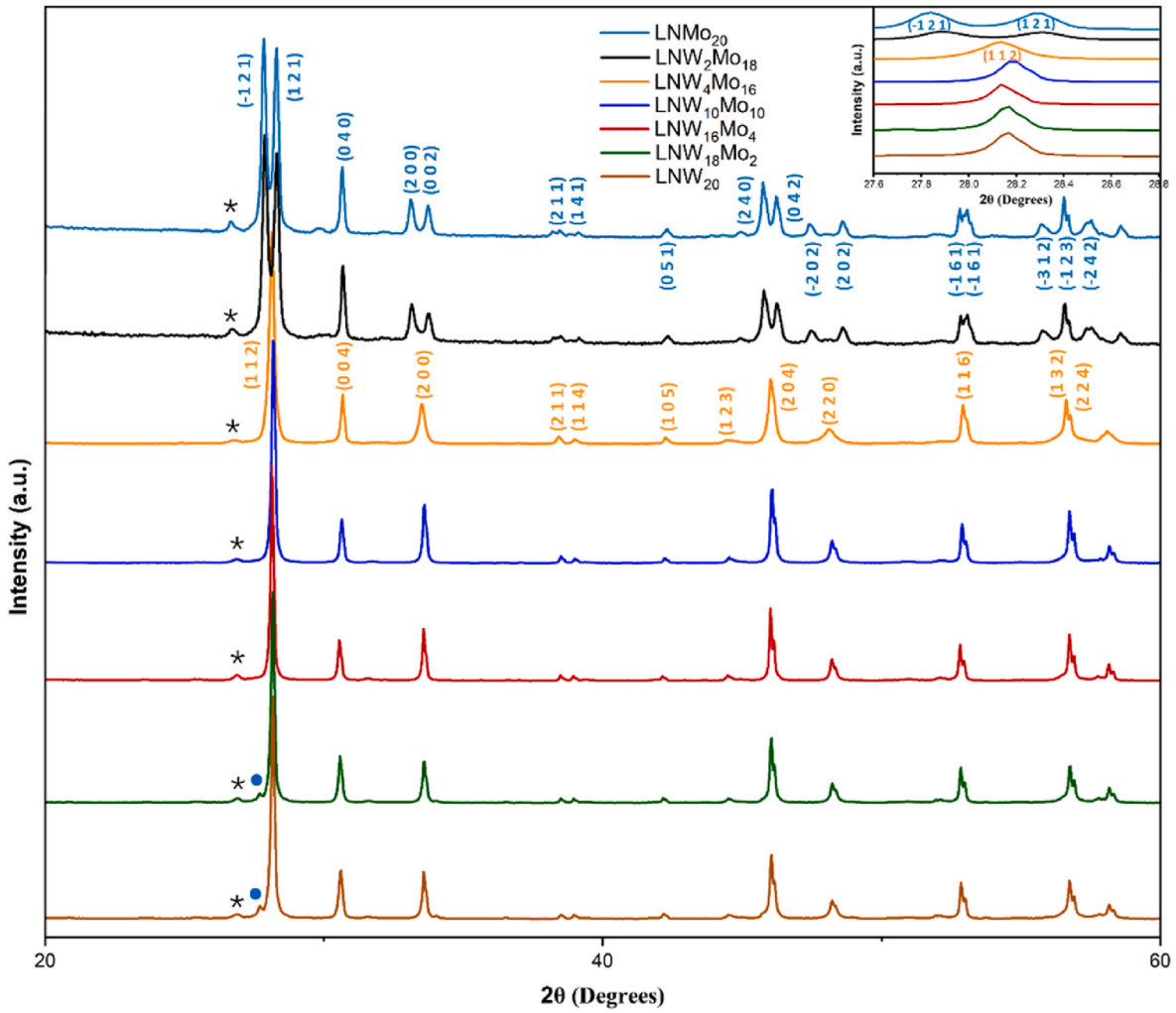

Fig. 1. XRD patterns of $LaNb_{0.8}W_xMo_{0.2-x}O_{4.1}$, displayed as a function of increasing concentration of W from top to bottom. Lattice planes in monoclinic fergusonite phase of $LNMo_{20}$ are labelled in blue, while lattice planes of the tetragonal scheelite phase of LNW_4Mo_{16} are labelled in orange. Peaks corresponding to modulated structures are marked by asterisk. Impurities in LNW_{20} and $LNW_{18}Mo_2$ are $La_2W_2O_9$, marked as blue dots. Change of main peaks are exhibited in top right corner inset. Reference PDF patterns are 01-085-3914 (monoclinic phase $LaNbO_4$) [25], 01-085-3919 (tetragonal phase $LaNbO_4$) [25], and 00-034-0652 ($La_2W_2O_9$) [26], respectively.

replaced by W^{6+} (0.56 Å in 4-coordinate) [27], while the plateau region above x = 0.16 could be attributed to the emergence of the W-rich impurity $La_2W_2O_9$, confirmed in XRD patterns. The evolution of the $La_2W_2O_9$ phase indicates that there is a solubility limit at the x = 0.16 composition. In addition, the *a* lattice parameter in Fig. 2 (c) remained stable with negligible change over the entire tetragonal regime, which suggests the doping ratio does not significantly impact the tetragonal lattice structure along the *a* axis.

Fig. 3 shows the phase diagram constructed from the VT-XRD data from room temperature to 900 °C. A clear decrease of monoclinic and tetragonal phase transition temperature was observed as the concentration of W increased from $LNMo_{20}$ and reached a minimum at LNW_4Mo_{16} at around room temperature. However, the disappearance temperature of modulated structures decreased first with lower W dopants content (x = 0.00–0.04), when x ≥ 0.10, the modulated structure continuously existed from room temperature to 900 °C.

Fig. 4 shows the SAED patterns of $LNW_{18}Mo_2$. The modulated structure observed along the [010] zone axis was similar to the previous work reported for $LaNb_{0.88}W_{0.12}O_{4.06}$ [19]; however, a modulated structure was also observed along [1 $\bar{1}$ 1] zone axis, which has not previously been reported for this type of material [19] and was different from that found along the [010] axis, as the satellite reflections along this axis were only found in one direction. The emergence of a new modulated structure along [1 $\bar{1}$ 1] axis in $LNW_{18}Mo_2$ might relate to difference in phases, where $LNW_{18}Mo_2$ possessed a tetragonal phase at room temperature and $LaNb_{0.88}W_{0.12}O_{4.06}$, in previous research, was proven to be a monoclinic phase [19]. The modulation vectors were determined to be $\mathbf{q1} \approx 0.349\mathbf{a}^* + 0.344\mathbf{c}^*$ and $\mathbf{q2} \approx 0.175\mathbf{a}^* + 0.657\mathbf{c}^*$ along [010] zone axis. For the modulated structure along [1 $\bar{1}$ 1] axis, only one modulation vector $\mathbf{q} \approx 0.165\mathbf{a}^* + 0.329\mathbf{b}^* + 0.165\mathbf{c}^*$ was found. Therefore, the modulated structures observed along [010] and [1 $\bar{1}$ 1] zone axes were considered as (3 + 2) D and (3 + 1) D incommensurate modulated structure, respectively.

3.2. *Microstructure of $LaNb_{0.8}W_xMo_{0.2-x}O_{4.1}$ series*

The morphology of both surfaces and cross-sections was investigated by SEM (Fig. S1), and the analysis of the composition was conducted by EDX. All samples exhibited a dense structure and the density of the samples measured by the Archimedes method reached 90 % after sintering. As the fraction of W remained at a lower level (x ≤ 0.10), the appearances of the samples displayed similar characteristics, represented by LNW_2Mo_{18} in Fig. 5 (a) and (b). As shown in the surface image, Fig. 5 (a), several particles with approximately 10 μm diameters were

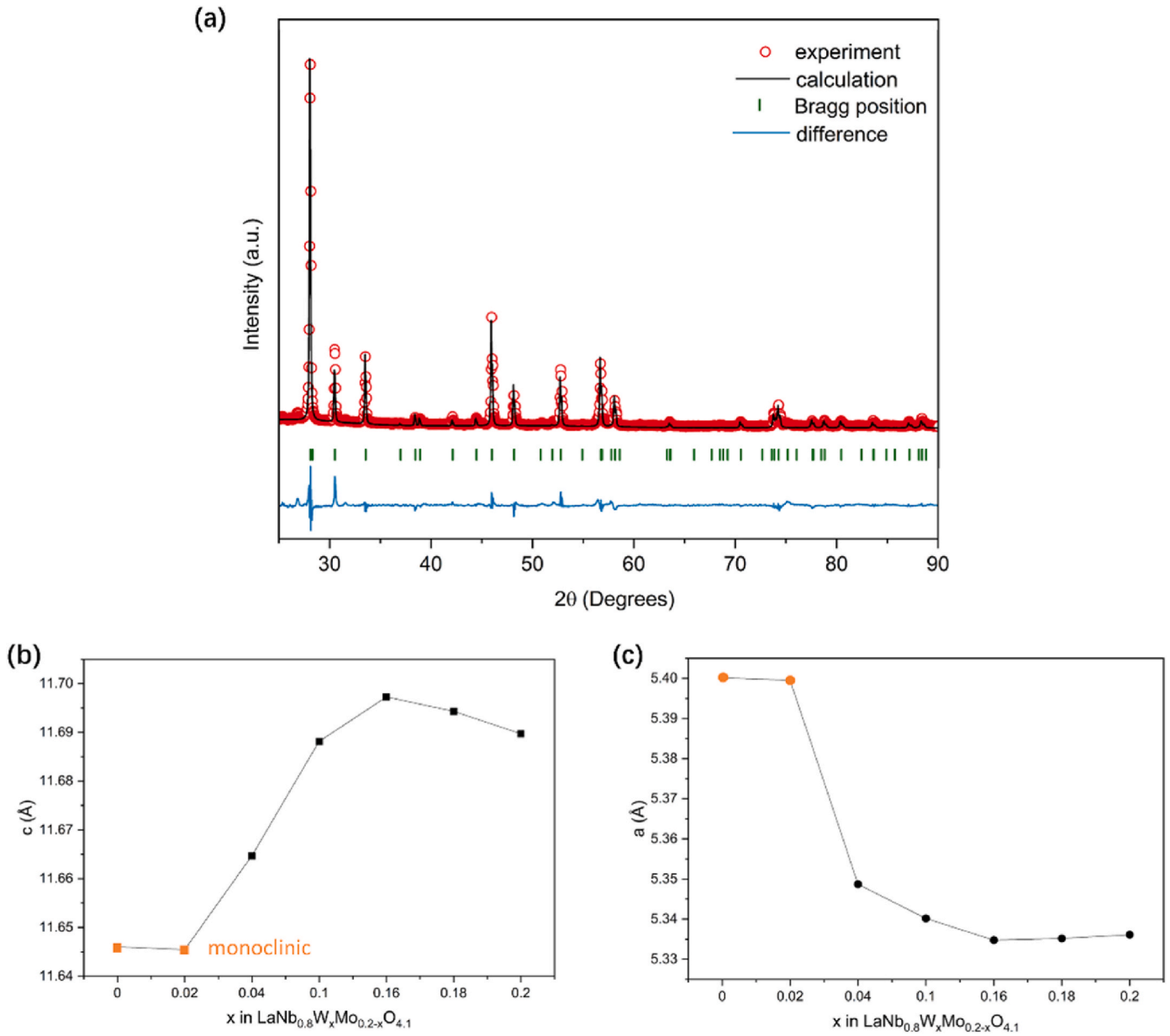

Fig. 2. (a) Plot of Rietveld refinement result of $LNW_{16}Mo_4$ at room temperature, GOF = 4.96, R_{wp} = 7.55 %. Bragg positions are based on the tetragonal phase $LaNbO_4$ (PDF #01-085-3919) [25]; lattice parameters of (b) *c* and (c) *a* in $LaNb_{0.8}W_xMo_{0.2-x}O_{4.1}$, error bars are smaller than the symbols.

surrounded by smaller particles with different ratios, and the difference in size among them was obvious but not significant. The cross-section images of samples with lower W fraction in Fig. 5 (b) exhibited compact structures, where fragments of grains could be observed.

For samples with higher W substitution level ($x > 0.10$), their morphologies were represented by LNW_{20} in Fig. 6. The appearance of the cross-section exhibited well-cut facets with sharp and clean edges, where the particle sizes increased evenly with limited small grains inlaid. This phenomenon was more obvious in the surface image, shown in Fig. 6 (b). The diameters of dominant particles were greater than 10 μm on average, accompanied by a few grains with much smaller size. Compared with samples with lower W fraction ($x \leq 0.10$), the difference in sizes among the particles was enhanced with increasing W content; where most particles had similar diameters (lower than 10 μm) with low W fraction, and dominant particles became larger (over 10 μm) with a few small grains (approximately 6 μm) in samples with elevated W content.

In the inset high magnification surface image in Fig. 6 (b), raised stripes located on the particle surfaces (marked as red circles) and grain boundaries (marked as blue ellipses) were observed in LNW_{20}. To verify the compositions of the stripes in different positions, point analysis EDX detailed in Table 1 determined that the ratio between La and W decreased from bulk (1:0.16) to stripes on grain boundaries (1:0.20) and stripes on bulk (1:0.26). The increased content of W might be attributed to segregation behaviour, where excess W cannot dissolve into the dominant grains, leading to the formation of W-rich phases in the grain boundaries. The W-rich secondary phase was identified as $La_2W_2O_9$ according to XRD patterns. Table 2 shows the EDX mapping results of the cross section of all samples; five spectra were recorded for each sample and the oxygen contents were excluded. The minor deficiency of W in LNW_{20} and $LNW_{18}Mo_2$ could also be related to the suggested segregation. The formation of secondary phases in grain boundaries might be attributed to the unstable stoichiometric grains which promoted the diffusion of W along grain boundaries in annealing [28].

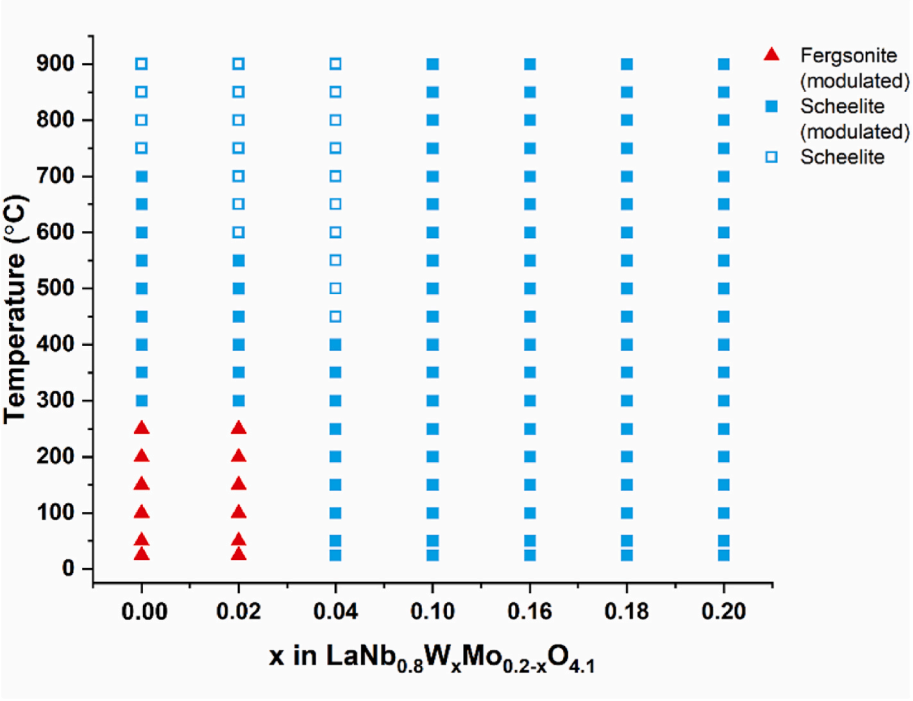

Fig. 3. The phase diagram of $LaNb_{0.8}W_xMo_{0.2-x}O_{4.1}$ from room temperature to 900 °C.

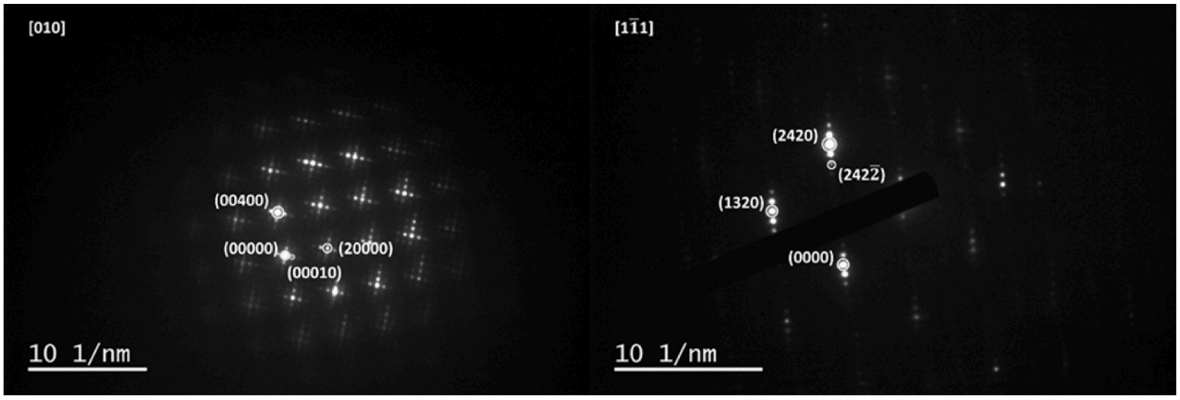

Fig. 4. SAED patterns along the zone axis [010] and [1 $\bar{1}$ 1] of $LNW_{18}Mo_2$ highlighting the modulation of the supercell.

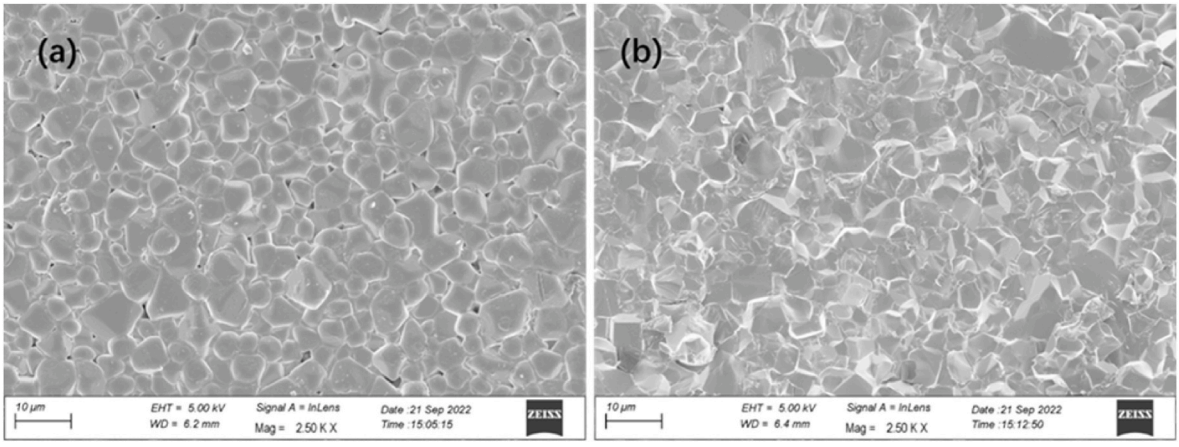

Fig. 5. SEM images of LNW_2Mo_{18} of (a) surface and (b) cross-section.

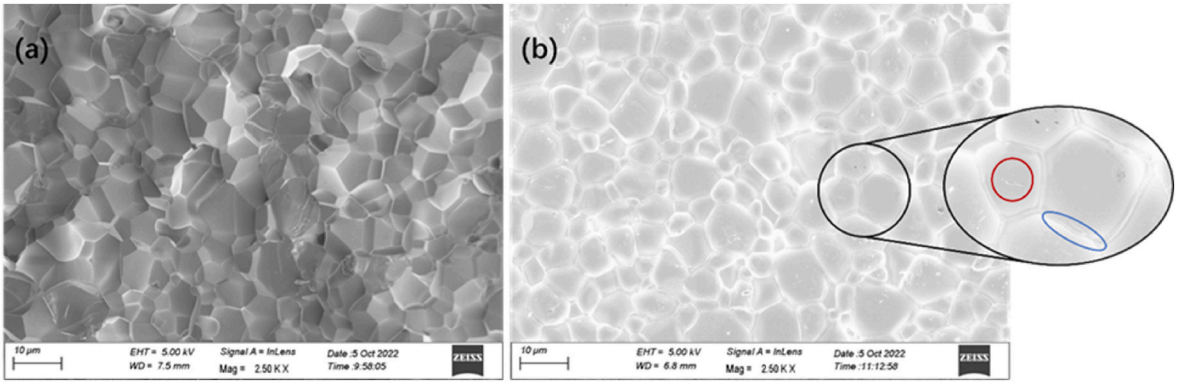

Fig. 6. SEM images of (a) cross-section and (b) surface morphologies of LNW_{20}. With zoomed-in image obtained at ×5000 magnification. Secondary phases are marked as red and blue circles in different position.

Table 1
Element ratios of different surface profiles determined by EDX.

	Position	Average ratio (La:W)
$LaNb_{0.8}W_{0.2}O_{4.1}$	Stripe on bulk	1:0.26
	Stripe on grain boundaries	1:0.20
	Bulk	1:0.16

Table 2
Normalized atomic fractions of cations of $LaNb_{0.8}W_xMo_{0.2-x}O_{4.1}$ series.

	La (%)	Nb (%)	W (%)	Mo (%)
$LNMo_{20}$	50.3 ± 0.4	40.2 ± 0.1	–	9.4 ± 0.1
Theoretical	50.00	40.00	–	10.00
LNW_2Mo_{18}	50.1 ± 0.7	40.6 ± 0.1	0.9 ± 0.5	8.4 ± 0.2
Theoretical	50.00	40.00	1.00	9.00
LNW_4Mo_{16}	49.3 ± 0.7	40.9 ± 0.6	1.9 ± 0.5	7.9 ± 0.2
Theoretical	50.00	40.00	2.00	8.00
$LNW_{10}Mo_{10}$	49.0 ± 0.3	41.3 ± 0.1	4.9 ± 0.2	4.8 ± 0.1
Theoretical	50.00	40.00	5.00	5.00
$LNW_{16}Mo_4$	50.1 ± 0.4	40.5 ± 0.2	7.5 ± 0.1	1.9 ± 0.1
Theoretical	50.00	40.00	8.00	2.00
$LNW_{18}Mo_2$	50.8 ± 0.7	40.3 ± 0.2	7.9 ± 0.1	0.9 ± 0.1
Theoretical	50.00	40.00	9.00	1.00
LNW_{20}	48.8 ± 0.3	41.9 ± 0.2	9.3 ± 0.1	–
Theoretical	50.00	40.00	10.00	–

3.3. Electrical properties of $LaNb_{0.8}W_xMo_{0.2-x}O_{4.1}$ series

An Arrhenius plot reflecting total conductivities of the $LaNb_{0.8}W_xMo_{0.2-x}O_{4.1}$ series measured in flowing compressed air from 600 °C to 900 °C, are shown in Fig. 7. A Nyquist plot of $LNMo_{20}$ is shown in the supporting information as an example of the fitting approach used to extract the conductivity data. (Figure S2). The conductivities of Mo-rich samples ($x < 0.10$) were approximately one order of magnitude higher than W-rich samples ($x > 0.10$) and the W-rich samples all exhibited similar conductivities. The similar conductivities of W-rich samples might be related to the segregation behaviour of W and formation of the secondary phase. Increased W ions tended to segregate at grain boundaries or surfaces of primary particles instead of diffusing into lattice structures, leading to identical chemical compositions; therefore, the electrochemical properties might appear with similar features. Two possible conclusions can be generated from the trend of conductivities. Mo dopants dominated the electrochemical performance since conductivity enhanced with increasing Mo concentration, where $LNMo_{20}$ exhibited highest conductivities, except at 665 °C. Alternatively, in the phase diagram, modulated structures disappeared in Mo-rich samples in the high temperature regime and only existed in the remaining compositions, indicating that the modulated structure might negatively influence ionic conductivity.

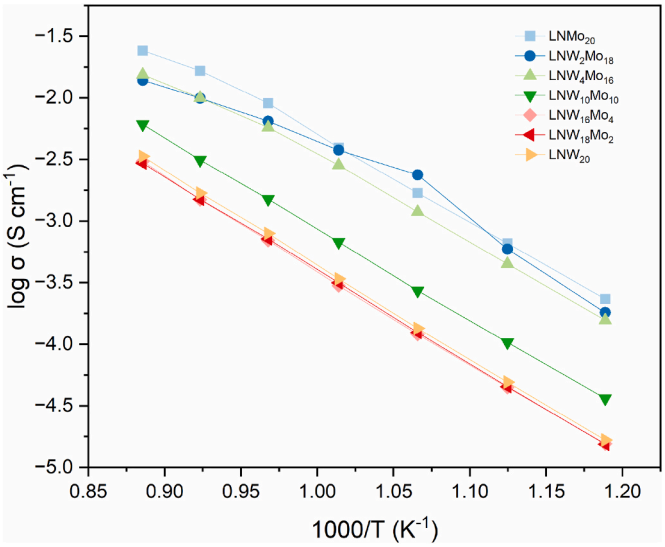

Fig. 7. Total conductivities of the $LaNb_{0.8}W_xMo_{0.2-x}O_{4.1}$ series in the 550 °C–900 °C temperature regime.

Close inspection revealed changes in the slopes of the conductivity plot at elevated temperature in the Mo-rich samples ($x \leq 0.04$), correlating to changes in activation energy of ion hopping, especially in LNW_2Mo_{18}. The detailed analysis of the activation energy change of LNW_2Mo_{18} is discussed in section 3.4.

Extracting the conductivities at 856 °C, the relationship between unit cell volumes and conductivities of the $LaNb_{0.8}W_xMo_{0.2-x}O_{4.1}$ series is clearly exhibited in Fig. 8, indicating total conductivity was approximately proportional to the volume of the unit cell. Table S2 summarizes the refined parameters for all materials recorded at 850 °C from VT-XRD. The phenomenon above verified that a smaller lattice could hinder the transportation of charge carriers, which could reduce total conductivity [18]. As the ionic radius of W^{6+} is larger than Mo^{6+}, the volume should increase with increasing W content in this series of materials. However, the unit cell volume displayed an unusual trend at 850 °C, where 2 different regions could be distinguished. The volumes of Mo-rich samples ($x < 0.10$) were higher than the volumes of W-rich samples ($x > 0.10$). The rapid decrease of volume happened from $x = 0.04$ to $x = 0.16$ and then the volume became stable afterwards. Combined with Fig. 3, all Mo-rich samples possessed unmodulated structures at 850 °C; however, all W-rich samples possessed modulated structures.

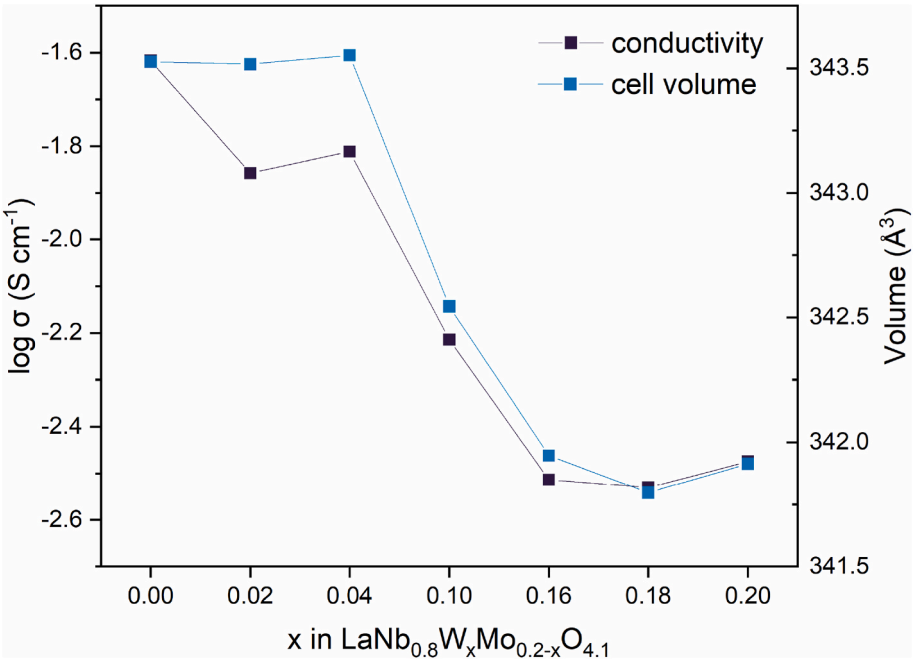

Fig. 8. Conductivities and unit cell volumes of $LaNb_{0.8}W_xMo_{0.2-x}O_{4.1}$ series at around 850 °C, error bars are smaller than the symbols.

Therefore, the mechanism of volume reduction could be related to the existence of a modulated structure, which also led to negative effects to the conductivities of the materials.

3.4. Detailed analysis of $LaNb_{0.8}W_{0.02}Mo_{0.18}O_{4.1}$

Given the high conductivity and distinctive phase transition aside from other components, detailed analysis of the LNW_2Mo_{18} phase is developed in this section. VT-XRD patterns collected from 25 °C to 900 °C were generated, recording phase change and lattice parameters in Fig. 9. The regions of different phase are marked by dashed lines. Fig. S3 shows the XRD patterns recorded around the temperature of the disappearance of the modulated structure of LNW_2Mo_{18}. The average coefficient of volumetric thermal expansion, $\alpha_{V,}$ was 36.3 × 10^{-6} K^{-1}. The α_V of LNW_2Mo_{18} was larger than typical electrode materials such as Ni-YSZ (10.3-14.1 × 10^{-6} K^{-1}) [29]. LNW_2Mo_{18} experienced a complete phase transition process from monoclinic to tetragonal at 300 °C, and the absence of a modulated structure started from 600 °C. As the structure approached the tetragonal transformation temperature point from 25 °C, lattice parameter *a* and *b* in the monoclinic phase continually decreased and merged, becoming the *a* parameter in the tetragonal phase, while *c* increased over the entire test regime. In the tetragonal region, lattice parameter *a* and *c* approximately linearly grew with β fixed at 90°. The volume of the unit cell maintained a steady linear growth in all phase regions. Compared with the parent material, $LaNb_{0.8}Mo_{0.2}O_{4.1}$, reported previously, both lattice parameters and volumes in the tetragonal phase (above 300 °C) maintained good consistency, however it was previously reported that a tetragonal structure formed at room temperature with a hysteretic effect producing a modulated monoclinic structure in the $LaNb_{0.8}Mo_{0.2}O_{4.1}$ at temperatures below 200 °C [15].

Fig. 10 shows the SAED patterns recorded along the [101] zone axis. The modulated structure of LNW_2Mo_{18} was similar to that observed in $LNW_{18}Mo_2$ mentioned above, as only one modulation vector $\mathbf{q} \approx 0.237\mathbf{a}^* + 0.237\mathbf{c}^*$ was required to index it.

Close examination of the electrochemical properties of LNW_2Mo_{18} revealed the change of activation energy of ion hopping, illustrated in Fig. 11. In order to get sufficient data points for the linear regression to calculate the activation energy, two additional temperature points at 475 °C and 520 °C were measured for LNW_2Mo_{18}. The activation energy decreased from $E_2 = 1.80$ eV to $E_1 = 0.85$eV at 665 °C. This temperature was also in the temperature regime with the absence of a modulated structure. A similar phenomenon has also been found in 10 % Mo substituted $LaNbO_4$, as the activation energy decreased from 1.53 eV to 0.64 eV with a transition of modulated structure to unmodulated structure [21]. Ion transport generated by thermal excitation should exhibit reduced activation energy, reflecting increasing conductivity. Fig. S4 shows the relationship between unit cell volumes (the refined parameters for all materials at 650 °C from VT-XRD are summarized in Table S3) and conductivities of $LaNb_{0.8}W_xMo_{0.2-x}O_{4.1}$ series at around 650 °C, which was similar to the relationship shown in Fig. 8. Given the coincidence of phase and energy change, it can be suggested that modulated structures might negatively impact the total conductivity because of the effect of decreasing the unit cell volume; however, further investigation is necessary to fully verify this. Also, other possibilities such as changing of charge carriers might be related to the energy decrease since the electrochemical reactions in the conduction process are not yet confirmed.

4. Conclusion

The strategy of co-doping W and Mo on Nb sites in the $La(Nb_{1-x}Mo_x)O_4$ phase can successfully reduce the phase transition temperature and stabilize a tetragonal phase at room temperature. As the fraction of W increased, the difference of particle sizes became significant, and the W-rich secondary phase formed in samples which contain 18 % W and above. Also, the volume expansion was observed along the c direction with elevated W fraction. The co-doping can also facilitate the emergence of modulated structures from room temperature to 900 °C with 10 % fraction of W and above.

For the relationship between conductivity and structure, the fraction of Mo dominates the electrochemical performance where the sample with highest Mo fraction exhibits the highest total conductivity. In addition, total conductivity is proportional to the volume of unit cell since the reduced lattice volume can suppress the diffusion pathways for oxide ion transportation.

For the tetragonal phase materials, it is suggested that modulated structures could be observed not only in one zone axis, and both (3 + 1)

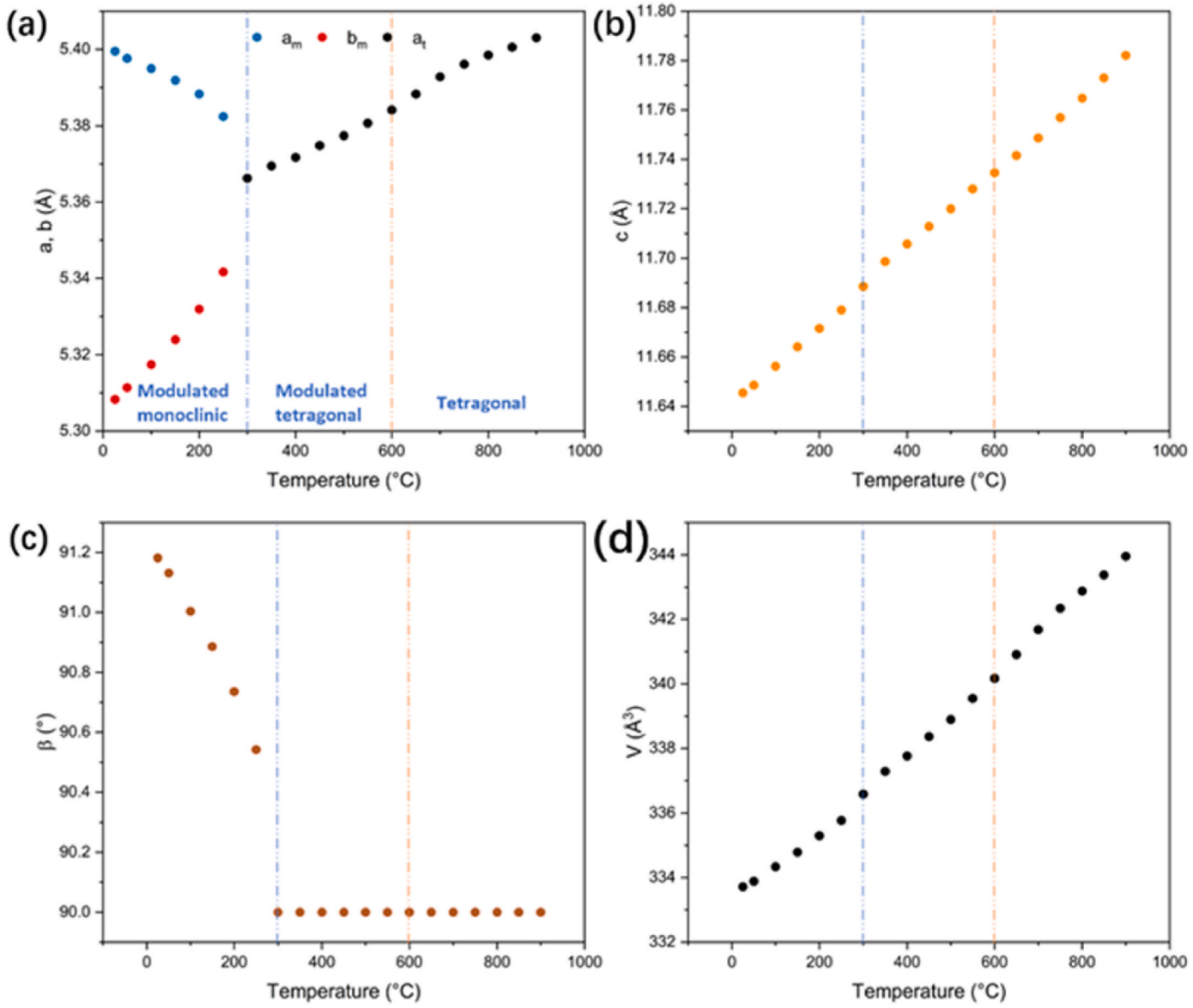

Fig. 9. Lattice parameters of (a) *a* and *b*, (b) *c*, (c) β, (d) volume of unit cell, derived for LNW_2Mo_{18} within the temperature range 25 °C–900 °C, collected by VT-XRD and computed from Rietveld refinement. "m" symbolizes monoclinic phase and "t" is tetragonal phase. Error bars are smaller than symbols.

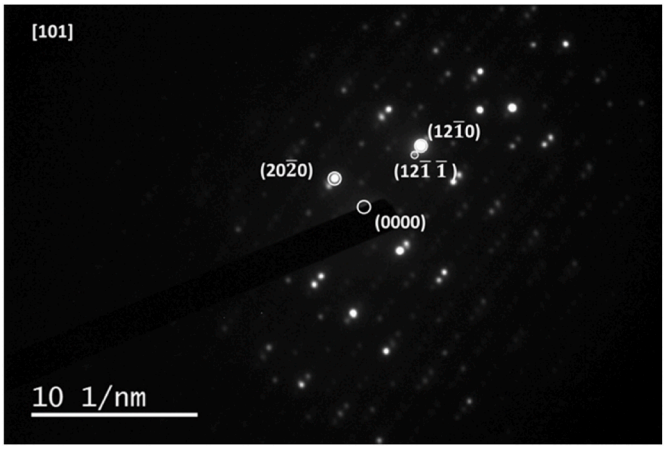

Fig. 10. SAED patterns of along the zone axis [101]* of LNW2Mo18.

D and (3 + 2) D modulated structures could exist. The existence of modulated structures might negatively impact the electrochemical performance since the samples with modulated structure possess smaller unit cell volumes and lower conductivities. The activation energy decreases when modulated structures disappear for $LaNb_{0.8}W_{0.02}Mo_{0.18}O_{4.1}$. These results will be useful for the development of a new type of oxide ion conductor in intermediate temperature ranges.

CRediT authorship contribution statement

Yidong Han: Writing – original draft, Methodology, Investigation, Formal analysis. **Siqi Li:** Writing – original draft, Investigation, Formal analysis. **Stephen Skinner:** Writing – review & editing, Supervision, Resources, Project administration, Funding acquisition, Data curation, Conceptualization.

Declaration of competing interest

The authors declare the following financial interests/personal relationships which may be considered as potential competing interests:

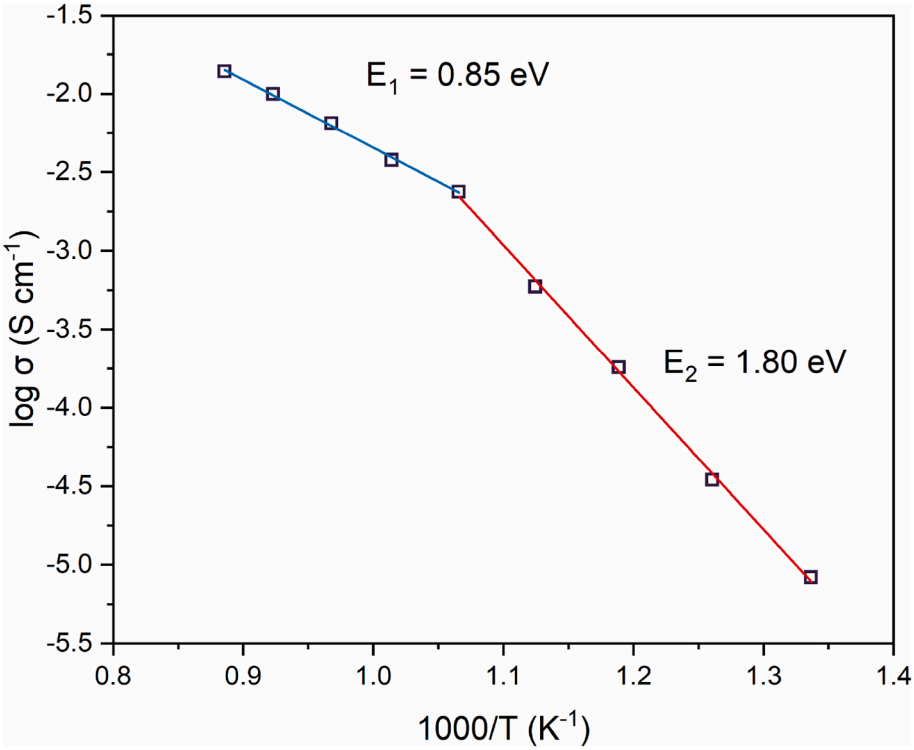

Fig. 11. Arrhenius plot of the total conductivity of $LaNb_{0.8}W_{0.02}Mo_{0.18}O_{4.1}$.

Stephen Skinner reports financial support was provided by Royal Academy of Engineering. If there are other authors, they declare that they have no known competing financial interests or personal relationships that could have appeared to influence the work reported in this paper.

Data availability

Data will be made available on request.

Acknowledgements

SJS thanks the Royal Academy of Engineering for the award of a Research Chair (RCSRF/2021-1243).

Appendix A. Supplementary data

Supplementary data to this article can be found online at https://doi.org/10.1016/j.jssc.2024.124590.

References

[1] R.M. Ormerod, Chem. Soc. Rev. 32 (2003) 17.
[2] A. Hawkes, I. Staffell, D. Brett, N. Brandon, Energy Environ. Sci. 2 (2009) 729.
[3] S.P.S. Badwal, S.S. Giddey, C. Munnings, A.I. Bhatt, A.F. Hollenkamp, Front. Chem. 2 (2014) 97517.
[4] L. Fan, C. Wang, M. Chen, B. Zhu, J. Power Sources 234 (2013) 154.
[5] H. Shi, C. Su, R. Ran, J. Cao, Z. Shao, Prog. Nat. Sci. Mater. Int. 30 (2020) 764.
[6] E. Fabbri, L. Bi, H. Tanaka, D. Pergolesi, E. Traversa, Adv. Funct. Mater. 21 (2011) 158.
[7] Z. Gao, L.V. Mogni, E.C. Miller, J.G. Railsback, S.A. Barnett, Energy Environ. Sci. 9 (2016) 1602.
[8] D.J.L. Brett, A. Atkinson, N.P. Brandon, S.J. Skinner, Chem. Soc. Rev. 37 (2008) 1568.
[9] R.J. Packer, S.J. Skinner, Adv. Mater. 22 (2010) 1613.
[10] R.J. Packer, E.V. Tsipis, C.N. Munnings, V.V. Kharton, S.J. Skinner, J.R. Frade, Solid State Ionics 177 (2006) 2059.
[11] R.J. Cava, R.S. Roth, T. Negas, H.S. Parker, D.B. Minor, J. Solid State Chem. 40 (1981) 318.
[12] S.W. Arulnesan, P. Kayser, J.A. Kimpton, B.J. Kennedy, J. Solid State Chem. 277 (2019) 229.
[13] H. Fjeld, K. Toyoura, R. Haugsrud, T. Norby, Phys. Chem. Chem. Phys. 12 (2010) 10313.
[14] K. Toyoura, Y. Sakakibara, T. Yokoi, A. Nakamura, K. Matsunaga, J. Mater. Chem. A 6 (2018) 12004.
[15] J.E. Auckett, L. Lopez-Odriozola, S.J. Clark, I.R. Evans, J. Mater. Chem. A 9 (2021) 4091.
[16] M.A. Laguna-Bercero, R.D. Bayliss, S.J. Skinner, Solid State Ionics 262 (2014) 298.
[17] C. Li, S.S. Pramana, R.D. Bayliss, C.P. Grey, F. Blanc, S.J. Skinner, Chem. Mater. 32 (2020) 2292.
[18] C. Li, R.D. Bayliss, S.J. Skinner, Solid State Ionics 262 (2014) 530.
[19] C. Li, S.S. Pramana, S.J. Skinner, Dalton Trans. 48 (2019) 1633.
[20] Y. Cao, N. Duan, X. Wang, B. Chi, Jian Pu, L. Jian, J. Eur. Ceram. Soc. 35 (2015) 1979.
[21] Y. Han, S.J. Skinner, Mater. Adv. 4 (2023) 3759.
[22] Y. Cao, B. Chi, J. Pu, L. Jian, J. Eur. Ceram. Soc. 34 (2014) 1981.
[23] Y. Jiazhen, Z. Yue, H. Wanxia, T. Mingjin, Thin Solid Films 516 (2008) 8554.
[24] B. H. Toby, R. B. Von Dreele, *urn:issn*:0021-8898 2013, 46, 544.
[25] P. Sarin, R.W. Hughes, D.R. Lowry, Z.D. Apostolov, W.M. Kriven, J. Am. Ceram. Soc. 97 (2014) 3307.
[26] N.P. Sabalisck, J. López-Solano, C. Guzmán-Afonso, D. Santamaría-Pérez, C. González-Silgo, A. Mujica, A. Muñoz, P. Rodríguez-Hernández, S. Radescu, X. Vendrell, L. Mestres, J.A. Sans, F.J. Manjón, Phys. Rev. B Condens. Matter 89 (2014) 174112.
[27] R. D. Shannon, C. T. Prewitt, IUCr, urn:issn:0567-7408 1970, 26, 1046.
[28] C. Li, S.S. Pramana, N. Ni, J. Kilner, S.J. Skinner, ACS Appl. Mater. Interfaces 9 (2017) 29633.
[29] D.A. Osinkin, D.I. Bronin, S.M. Beresnev, N.M. Bogdanovich, V.D. Zhuravlev, G. K. Vdovin, T.A. Demyanenko, J. Solid State Electrochem. 18 (2014) 149.